www.sciencemag.org/content/356/6340/837/suppl/DC1

Supplementary Materials for

Quantum sensing with arbitrary frequency resolution

J. M. Boss,* K. S. Cujia,* J. Zopes, C. L. Degen†

*These authors contributed equally to this work.
†Corresponding author. Email: degenc@ethz.ch

Published 26 May 2017, *Science* **356**, 837 (2017)
DOI: 10.1126/science.aam7009

This PDF file includes:

Materials and Methods

Experimental setup

Experiments were performed with a custom-built confocal microscope equipped with a green 532 nm excitation laser and a single photon detector, as well as microwave and radio frequency sources to control the NV center spin and the ^{15}N nuclear spin, respectively. The NV centers were created by ^{15}N^{+} ion implantation at an energy of 5 keV and subsequent annealing at 850° C. We chose the ^{15}N species to discriminate implanted NV centers from native (^{14}N) NV centers. However, the isotope species played no role for the present experiments. We etched nano-pillars into the diamond surface *(31, 32)* to increase the photon collection efficiency by a factor of 10 to 15 compared to a non-structured diamond surface. The continuous wave (CW) photon count rate was between 400 and 700 kC/s.

Microwave pulses were synthesized on an arbitary waveform generator (Tektronix AWG5012C) and upconverted to $\sim 10\,\mathrm{GHz}$ using a local oscillator (Hittite HMCT2100) and a single-sideband mixer (IQ0618, Marki microwave). Radio-frequency pulses were synthesized on a second arbitrary waveform generator (NI 5421, National Instruments). Microwave and radio-frequency pulses were amplified separately and then combined using a bias T. The pulses were delivered to the NV center using a coplanar waveguide (CPW) deposited on a quartz cover slip in a transmission line geometry. The transmission line was terminated by an external $50\,\Omega$ load.

A cylindrical permanent magnet was used to create a magnetic bias field of $450-500\,\mathrm{mT}$ at the location of the NV center. At this high bias field repolarization of the ^{15}N nucleus under optical illumination *(33)* is greatly suppressed. This allowed for a large number ($n > 1000$) of repetitive nuclear spin readouts to be performed. The magnetic field direction was aligned with the NV symmetry axis by adjusting the relative location of the permanent magnet. The alignment was optimized by maximizing the CW photon count rate and by minimizing the depolarization of ^{15}N nuclear spin states under repetitive readout. The magnetic field drifted by typically a few Gauss over the course of an experiment, corresponding to a variation in the EPR frequency of $\sim 1\,\mathrm{MHz}$. Because the drifts were slow, we could continuously track the EPR resonance during a measurement and adjust the microwave excitation frequency. In this way, the detuning between the EPR resonance frequency and the microwave frequency could be reduced to $< 100\,\mathrm{kHz}$.

Sensing sequence

A schematic of the sensing sequence is shown in Fig. S1.

To arm the sensor, we initialized both the electronic and the ^{15}N nuclear spins. The electronic spin was initialized by means of a $\sim$ 1.5 μs laser pulse. The nuclear ^{15}N spin was initialized by a sequence of two c-NOT gates followed by a laser pulse to reset the electronic spin. The initialization efficiency was not measured, but is expected to be $> 80\%$ for the electronic spin *(34)* and $> 70\%$ for the nuclear spin *(35)*, respectively. The first (electronic) c-NOT gate included a selective microwave π pulse on the lower hyperfine resonance ($\sim 9922.22\,\mathrm{MHz}$) of the electronic $m_S = 0 \leftrightarrow m_S = -1$ transition. The second (nuclear) c-NOT gate included a selective radio-frequency π pulse on the higher frequency hyperfine resonance ($\sim 1.97\,\mathrm{MHz}$) of the nuclear $m_I = -1/2 \leftrightarrow m_I = +1/2$ transition. The duration of the selective microwave pulse was $\sim 290\,\mathrm{ns}$ and the duration of the selective radio-frequency pulse was $\sim$ 40 μs.

Quantum lock-in detection was implemented by a Carr-Purcell-Meiboum-Gibbs (CPMG) sequence of periodic microwave π pulses. The sequence consisted of K pulses with an interpulse delay τ. The interpulse delay was chosen to approximately match the expected a.c. signal frequency $f_{\rm ac}$ as $f_{\rm ac} \approx m/(2\tau)$, where $m = 1, 3, 5, ...$ is the harmonic order of the sequence. The value of τ can be determined either by a prior knowledge about $f_{\rm ac}$, or by scanning a range of τ values. The total duration of the CPMG sequence was $t_{\rm a} = K\tau$. To optimize the sequence, we adjusted the number of pulses K so that the maximum phase pick-up was ~ 0.5.

The readout of the final NV state was performed indirectly via a repetitive quantum non-demolition measurement of the ^{15}N nuclear spin *(35)*. For this purpose, the final electronic spin state was stored in the ^{15}N spin state using a nuclear c-NOT gate and a laser pulse for resetting the electronic spin state. Next, the nuclear spin state was read out using an electronic c-NOT gate followed by a short ($600 - 800\,$ns) laser pulse. The nuclear read-out was repeated n times (with n up to 2,000). The duration of one nuclear readout was $t_{\rm r} \approx 2.32$ μs. The total readout duration was $n \times 2.32$ μs. The integrated counts over n repetitive readouts correspond to a single sample record y_k.

The sensing sequence incorporated an additional delay time $t_{\rm d}$. This delay time was used for initialization and for accommodating a separate short pulse sequence to continuously track the NV resonance frequency and correct for drifts. The delay time was also used to adjust the sampling time $t_{\rm s} = t_{\rm a} + t_{\rm r} + t_{\rm d}$ in the compressed sampling experiment.

Experimental parameters

The following tables give the parameters that went into the measurements shown in Figures 2, 3, and 4.

Parameters for Figure 2A-B

B field	546.59 mT
NV initialization laser pulse	2 μs
Repetitive readout laser pulse	600 ns
Selective electronic pulse duration	290 ns
Selective nuclear pulse duration	30 μs
CPMG pulses K	32
CPMG duration $t_{\rm a}$	26.622 μs
Sampling period $t_{\rm s}$	4.21152 ms
Number of repetitive readouts n	1000

We have evaluated the amplitude of the a.c. magnetic field detected in this experiment. The CPMG duration $t_{\rm a}$ was chosen such that the amplitude of the probability was ~ 0.25. According to Eq. (2), the amplitude of the phase was ~ 0.5. According to Eq. (1), the amplitude of the signal Ω was $\sim 2\pi \times 4.7\,$kHz. The amplitude of the a.c. magnetic field was $\Omega/\gamma_{\rm e} \sim 170\,$nT, where $\gamma_{\rm e} = 2\pi \times 28\,$GHz/T is the electron gyromagnetic ratio.

Parameters for Figures 2C-D and Figure S3

B field	$456.54\,\mathrm{mT}$
NV initialization laser pulse	$1\ \mu\mathrm{s}$
Repetitive readout laser pulse	$800\,\mathrm{ns}$
Selective electronic pulse duration	$290\,\mathrm{ns}$
Selective nuclear pulse duration	$40\ \mu\mathrm{s}$
CPMG pulses K	16
CPMG duration t_a	$6.654\ \mu\mathrm{s}$
Sampling period t_s	$1.31524\,\mathrm{ms}$
Number of repetitive readouts n	498

Parameters for Figure 3

B field	$456.54\,\mathrm{mT}$
NV initialization laser pulse	$1\ \mu\mathrm{s}$
Repetitive readout laser pulse	$800\,\mathrm{ns}$
Selective electronic pulse duration	$290\,\mathrm{ns}$
Selective nuclear pulse duration	$40\ \mu\mathrm{s}$
CPMG pulses K	16
CPMG duration t_a	$6.654\ \mu\mathrm{s}$
Sample records N	385263
Sampling period t_s	$1.31524\,\mathrm{ms}$ (for datapoints where $n \leq 498$)
Sampling period t_s	$5.16468\,\mathrm{ms}$ (for datapoints where $n > 498$)

We have used this experiment to determine the optimum SNR for a one-hour measurement interval. In the plot, the SNR at the threshold gain of $C_\mathrm{thresh} = 27$ ($n = 260$) was $1.0 \cdot 10^3$. The duration of this measurement was $T = Nt_\mathrm{s} = 294\,\mathrm{s}$, where $N = 3.85 \cdot 10^5$ was the number of samples and $t_\mathrm{s} = 0.763\,\mathrm{ms}$ was the sampling period. According to Eq. (6), this converts to an SNR of $1.0 \cdot 10^3 \times (1\,\mathrm{h})/T = 1.2 \cdot 10^4$ for a one-hour interval.

Parameters for Figure 4

B field	$456.69\,\mathrm{mT}$
NV initialization laser pulse	$1\ \mu\mathrm{s}$
Repetitive readout laser pulse	$800\,\mathrm{ns}$
Selective electronic pulse duration	$290\,\mathrm{ns}$
Selective nuclear pulse duration	$40\ \mu\mathrm{s}$
CPMG pulses K	16
CPMG duration t_a	$19.965\ \mu\mathrm{s}$
Number of repetitive readouts n	498

The following table gives the sampling rates $f_{\mathrm{s}}^{(i)}$ for the spectra shown in Fig. 4A:

i	$f_{\mathrm{s}}^{(i)}$ (Hz)
1	752.6719855487
2	750.7507507508
3	749.4454103963
4	747.6747315848
5	746.0904858541
6	743.7819826253
7	742.6772027806

Supplementary Text 1: Details of the quantum lock-in protocol

Our implementation of the quantum lock-in protocol is based on a Carr-Purcell-Meiboum-Gibbs (CPMG)-type sequence of K periodic π-pulses. Assuming the qubit is in the $|0\rangle$ state (the $m_S = 0$ spin state) at the beginning of the sequence, the first $(\pi/2)_Y$-pulse rotates it into the $|{+X}\rangle = \frac{1}{\sqrt{2}}(|0\rangle + |1\rangle)$ state, where $|1\rangle$ corresponds to the $m_S = -1$ spin state. The qubit then evolves under a series of π-pulses with inter-pulse delays τ. At the end of the CPMG sequence, the resulting state is rotated again by $\pi/2$ but this time around the X axis. This leaves the qubit in the superposition state

$$|\psi\rangle \equiv \sin\left(\frac{\phi}{2} + \frac{\pi}{4}\right)|0\rangle - \cos\left(\frac{\phi}{2} + \frac{\pi}{4}\right)|1\rangle \ , \tag{S1}$$

where we omit a global phase. ϕ is the phase acquired by the qubit during the decoupling sequence. The readout projects the qubit onto either $|0\rangle$ or $|1\rangle$. The probability p for projection onto $|1\rangle$ is

$$p = |\langle 1|\psi\rangle|^2 = \frac{1}{2}\left(1 - \sin\phi\right) . \tag{S2}$$

Next we consider how the phase ϕ relates to the a.c. signal. We assume that the a.c. signal is given by the oscillating field

$$x(t) = \Omega\cos(2\pi f_{\mathrm{ac}} t + \alpha), \tag{S3}$$

where Ω is the amplitude (in units of angular frequency), f_{ac} the frequency, and α the initial phase of the signal at time $t = 0$ after the first $\pi/2$ pulse was applied. For the specific situation of our experiment, where the qubit is an electronic spin, the a.c. signal is generated by a magnetic field,

$$x(t) = \gamma_{\mathrm{e}} B_z \cos(2\pi f_{\mathrm{ac}} t + \alpha) \ , \tag{S4}$$

where $B_z = \Omega/\gamma_{\mathrm{e}}$ represents the magnetic field component along the qubit's quantization axis, and $\gamma_{\mathrm{e}} = 2\pi \times 28\,\mathrm{GHz/T}$ is the electron gyromagnetic ratio. For simplicity, we in the following assume that $\alpha = 0$ because we always measure a relative time. The phase acquired by the qubit is then given by

$$\phi(t) = \int_0^{t_{\mathrm{a}}} dt' x(t + t') g(t') \ , \tag{S5}$$

where $g(t') = (-1)^{[t'/\tau]}$ is the modulation function *(2)* of the CPMG sequence (see Fig. S2). For an even number of pulses K, the phase accumulated under the modulation function of the CPMG sequence is *(2)*

$$\phi(t) = -\frac{8}{2\pi f_{\mathrm{ac}}}\Omega\cos\left(2\pi f_{\mathrm{ac}}\left[t + \frac{1}{2}K\tau\right]\right)\frac{\sin\left(2\pi f_{\mathrm{ac}}\frac{K\tau}{2}\right)}{\sin\left(2\pi f_{\mathrm{ac}}\tau\right)}\sin\left(2\pi f_{\mathrm{ac}}\frac{\tau}{4}\right)^2 \sin\left(2\pi f_{\mathrm{ac}}\frac{\tau}{2}\right) . \tag{S6}$$

When the inter-pulse delay τ is approximately adjusted to the frequency of the a.c. signal, $\tau \approx m/(2f_{\mathrm{ac}})$ (where $m = 1, 3, 5, ...$ is the harmonic order), the above general formula simplifies to

$$\phi(t) = (-1)^q \frac{2t_{\mathrm{a}}}{m\pi}\Omega\cos(2\pi f_{\mathrm{ac}} t) = (-1)^q \frac{2t_{\mathrm{a}}}{m\pi} x(t), \tag{S7}$$

where $q = \frac{m-1}{2}$. As a result, the phase $\phi(t)$ is directly proportional to the instantaneous value of the signal $x(t)$. Thus, by using a series of quantum lock-in measurements, we can record how the ac signal $x(t)$ evolves with time.

To calculate the transition probability, we insert $\phi(t)$ into Eq. S2,

$$p(t) = \frac{1}{2}\left(1 - \sin\left[(-1)^q \frac{2t_\mathrm{a}}{m\pi} x(t)\right]\right) = \frac{1}{2}\left(1 - \sin\left[\phi_\mathrm{max}\cos(2\pi f_\mathrm{ac} t)\right]\right) . \tag{S8}$$

ϕ_max is the amplitude of the a.c. signal expressed in units of the accumulated phase,

$$\phi_\mathrm{max} = (-1)^q \frac{2t_\mathrm{a}\Omega}{m\pi} \quad \overset{m=1}{=} \quad \frac{2t_\mathrm{a}\Omega}{\pi} , \tag{S9}$$

where the last expression ($m = 1$) represents our experimental situation.

For small ϕ, the sine term is linear in ϕ and the probability is

$$p(t) \approx \frac{1}{2}\left(1 - \phi_\mathrm{max}\cos(2\pi f_\mathrm{ac} t)\right) , \tag{S10}$$

When several signals are present, the probability $p(t)$ simply is a linear combination of the individual contributions, as long as the maximum phase ϕ is within the linear range of the sine.

Conversely, when $\phi_\mathrm{max} \gtrsim 1$, the response of p becomes nonlinear *(20)*. Specifically, for a single signal with frequency f_ac and amplitude ϕ_max,

$$p(t) = \frac{1}{2} - \sum_{k=0}^{\infty} (-1)^k J_{2k+1}(\phi_\mathrm{max}) \cos\left[(2k+1)2\pi f_{ac} t\right] , \tag{S11}$$

where $J_k(\phi_\mathrm{max})$ is the Bessel function of first kind. The probability $p(t)$ now contains harmonics at $3f_\mathrm{ac}$, $5f_\mathrm{c}$, etc. of the original signal frequency f_ac whose amplitudes are given by Bessel functions. Fig. S4A shows simulated spectra for values of ϕ_max between 0.5 and 14. Fig. S4C further shows that the combined power of all harmonic peaks, given through $\sum_{k=0}^{\infty} J_{2k+1}^2(\phi_\mathrm{max})$, saturates as $\phi_\mathrm{max} \gtrsim 1$ and approaches 0.25 as $\phi_\mathrm{max} \to \infty$.

Finally, if several signals are present with ϕ_max in the nonlinear regime, frequency mixing occurs (Fig. S4B). Because of the harmonic generation and frequency mixing, spectra acquired in the nonlinear regime are difficult to interpret and it is advantageous to stay in the linear range of the sensor.

To confirm the theoretical analysis above, we recorded spectra for different values of ϕ_max exceeding the linear regime. Fig. S5A shows these measurements. We assigned the peaks in the spectra to their corresponding harmonic order. Thereby, we find harmonics up to the order $2k + 1 = 21$ for the measurement of the strongest signal where $\phi_\mathrm{max} = 21.6$. Furthermore, in Fig. S5B, we fitted the the peak height for the first 4 harmonics to their Bessel functions squared, finding good agreement with Eq. (S11).

Supplementary Text 2: Scaling of frequency estimation

In Fig. 2E of the main text we investigate the scaling of the uncertainty of the estimated center frequency with increasing total measurement time T. We find that the uncertainty scales as $T^{-1.5}$ if the intrinsic linewidth parameter γ_{int} of the signal is smaller than the frequency resolution $\delta f = 1/T$, and that it scales as $T^{-0.5}$ if γ_{int} is larger than δf. This section serves to motivate these two scaling laws.

We first consider the situation where the intrinsic linewidth of the spectral peak is larger than the frequency resolution, $\gamma_{\text{int}} > \delta f$. This situation leads to a $T^{-0.5}$ scaling for the uncertainty in the center frequency. We estimate the uncertainty by a least-squares fit to a Lorentzian. Let $h_\beta(f)$ be the model function for the Lorentzian where $\beta = (f_{\text{c}}, \gamma)$ are the model parameters, f_{c} the center frequency, and γ the linewidth parameter. The variance of the estimated parameters $\hat{\beta}_i$ $(i = 1, 2)$ can be estimated via the covariance matrix,

$$\Sigma = \left(J^T J\right)^{-1} \sigma_{\text{res}}^2 \,, \tag{S12}$$

where

$$J = \left(\frac{\partial h_{\hat{\beta}}\left(f_j\right)}{\partial \beta_i}\right)_{j,i} \tag{S13}$$

is the Jacobian matrix of the model function at the estimated parameter values for the measured frequencies f_j and

$$\sigma_{\text{res}}^2 = \frac{1}{N-2} \sum_{j=1}^{N} \left(h_j - h_{\hat{\beta}}(f_j)\right)^2 \tag{S14}$$

is the variance of the residuals (noise variance), respectively. $N = T/t_{\text{s}}$ is the number of samples and t_{s} is the sampling time. The variances of the individual model parameters are then the diagonal elements of the covariance matrix. Thus, the uncertainty in the estimated center frequency is given by the square root of the first diagonal element of the covariance matrix,

$$\sigma_{f_{\text{c}}} = \sqrt{\Sigma_{11}} = \sqrt{\left[\left(J^T J\right)^{-1}\right]_{11} \sigma_{\text{res}}^2} \,. \tag{S15}$$

Since the SNR saturates for peaks whose intrinsic linewidth is well resolved ($\gamma_{\text{int}} > \delta f$), we know that the variance of the residuals stays constant for longer measurement times (see Eq. (S38)). However, the number of resources (number of frequency points in the spectrum N) used for the fit increases linearly together with the measurement time T.

To find the scaling of the uncertainty, we have to evaluate the first diagonal element of $\left(J^T J\right)^{-1}$ in the limit of a well resolved linewidth,

$$\left(J^T J\right)^{-1} = \begin{pmatrix} \sum_{j=1}^{N} \left(\frac{\partial}{\partial f_{\text{c}}} h_{\hat{\beta}}(f_j)\right)^2 & \sum_{j=1}^{N} \left(\frac{\partial}{\partial \gamma} h_{\hat{\beta}}(f_j)\right) \left(\frac{\partial}{\partial f_{\text{c}}} h_{\hat{\beta}}(f_i)\right) \\ \sum_{j=1}^{N} \left(\frac{\partial}{\partial \gamma} h_{\hat{\beta}}(f_j)\right) \left(\frac{\partial}{\partial f_{\text{c}}} h_{\hat{\beta}}(f_j)\right) & \sum_{j=1}^{N} \left(\frac{\partial}{\partial \gamma} h_{\hat{\beta}}(f_j)\right)^2 \end{pmatrix}^{-1} . \tag{S16}$$

Since we assume $\gamma_{\text{int}} > \delta f$, we can approximate the sums with their corresponding integrals. For the first diagonal entry, we find

$$\left[\left(J^T J\right)^{-1}\right]_{11} = \frac{f_s}{2N} \underbrace{\left(\int_0^{\frac{f_s}{2}} \left(\frac{\partial}{\partial f_{\mathrm{c}}} h_{\hat{\beta}}(f)\right)^2 \mathrm{d}f\right)^{-1}}_{=u(\hat{\beta})} = \frac{f_s}{2N} \times u(\hat{\beta}) \,, \tag{S17}$$

where the factor $u(\hat{\beta})$ is assumed to be approximately constant, since the estimated parameters $\hat{\beta}$ are at a minimum. Hence, the uncertainty of the center frequency scales as

$$\sigma_{f_{\mathrm{c}}} \propto N^{-0.5} \propto T^{-0.5}. \tag{S18}$$

In the situation where the intrinsic linewidth is smaller than the frequency resolution, $\gamma_{\text{int}} < \delta f$, the approximation in Eq. (S17) is not valid. Furthermore, the number of resources for fitting the center frequency is not increasing with longer measurement times. We are given only three points in the spectrum to estimate the center frequency value: The point in the spectrum carrying most of the power and the two neighboring points left and right to that center peak. However, the SNR increases linearly and thus the relative noise variance decreases linearly. Therefore, the T^{-1} scaling of the frequency resolution given by the Fourier transformation is boosted by $T^{-0.5}$ due to the SNR scaling, resulting in a overall uncertainty scaling of

$$\sigma_{f_{\mathrm{c}}} \propto T^{-1.5} \,. \tag{S19}$$

Supplementary Text 3: Details of signal-to-noise ratio derivation

This section provides the theoretical background for the signal-to-noise ratio (SNR) presented in Eqs. (4-6) of the main manuscript. We repeat here Eq. (4) for reference,

$$\mathrm{SNR} \approx \frac{Y_j}{\sigma_Y}. \tag{S20}$$

Y_j is the height of a signal peak at frequency f_j in the power spectrum, and σ_Y is the standard deviation of the baseline noise evaluated in a frequency range where no signal is present. In the following we calculate the expectation values for Y_j and σ_Y based on Eqs. (2,3) of the main manuscript. This will lead us to Eq. (6) of the main manuscript.

In a first step, we calculate the expected signal that appears in the power spectrum for a time trace $\{y_k\}_{k=0}^{N-1}$ of photon counts, where y_k was sampled at times $t_k = kt_\mathrm{s}$, t_s is the sampling period and N is the number of samples. To compute the power spectrum we first perform a discrete Fourier transform (DFT) of the time trace and then calculate the absolute square of the individual components. The individual components of the power spectrum are given by

$$Y_j = |\hat{y}_j|^2 = \left| \sum_{k=1}^{N} y_k e^{-2\pi ikj} \right|^2 . \tag{S21}$$

Note that our definition of the DFT does not include any normalization by the number of points, *i.e.* , we do not normalize the DFT by N or $\sqrt{N}$. Therefore, the power in each component grows with the square of N. The expected power in component Y_j is

$$\begin{aligned}
\mathrm{E}\left[Y_j\right] &= \sum_{k=0,l=0}^{N-1} \mathrm{E}\left[y_k y_l\right] e^{-2\pi ikj} e^{2\pi ilj} && \text{(S22)}\\
&= \sum_{k=0,l=0}^{N-1} \mathrm{E}\left[y_k\right] \mathrm{E}\left[y_l\right] e^{-2\pi ikj} e^{2\pi ilj} + \sum_{k=0,l=0}^{N-1} \mathrm{cov}\left[y_k, y_l\right] e^{-2\pi ikj} e^{2\pi ilj} && \text{(S23)}\\
&= \underbrace{\left|\mathrm{E}\left[\hat{y}_j\right]\right|^2}_{\text{signal contribution}} + \underbrace{\sum_{k=0}^{N-1} \mathrm{var}(y_k)}_{\text{noise contribution}} . && \text{(S24)}
\end{aligned}$$

The last equation holds because any two samples at different times are independent. We find that the power contained in component Y_j is the sum of two contributions, one by the a.c. signal (first term) and one by the noise (second term). The expected noise contribution is given by

$$\sum_{k=0}^{N-1} \mathrm{var}(y_k) = N\sigma_y^2 \tag{S25}$$

where $\sigma_y^2 = \mathrm{var}(y_k)$ for any k. This term represent the noise floor in the spectrum that is unrelated to the a.c. signal. In particular, as we will show below, this noise floor is present at any frequency, and has no frequency dependence, *i.e.* , the noise floor is flat.

Next, we determine the noise entering the SNR. The noise is given by the standard deviation of Y_j,

$$\sigma_Y = \mathrm{std}\left(Y_j\right) . \tag{S26}$$

To calculate σ_Y, we consider a power spectrum of a random stationary process without any additional a.c. signal, *i.e.* , we assume $p(t_k) = 0.5$. We indicate quantities corresponding to this signal by a tilde, e.g. $\{\tilde{y}_k\}$ would be its time trace of measurement outcomes. Let $\tilde{R}_j$ and $\tilde{I}_j$ be the real and imaginary parts of $\hat{\tilde{y}}_j = \tilde{R}_j + i\tilde{I}_j$. Then, for large N, the central limit theorem implies that $\tilde{R}_j$ and $\tilde{I}_j$ have a normal distribution with zero mean and variance $\tilde{\sigma}^2$, where $\tilde{\sigma}^2$ is unknown. $\tilde{R}_j$ and $\tilde{I}_j$ are independent and identically distributed for $j < \frac{N}{2}$. We now write the power as sum of the power in the two quadratures

$$\tilde{Y}_j = \left|\hat{\tilde{y}}_j\right|^2 = \tilde{R}_j^2 + \tilde{I}_j^2. \tag{S27}$$

Furthermore, we realize that

$$\frac{1}{\tilde{\sigma}^2}\tilde{Y}_j = \frac{1}{\tilde{\sigma}^2}\tilde{R}_j^2 + \frac{1}{\tilde{\sigma}^2}\tilde{I}_j^2 \sim \chi^2(2) \tag{S28}$$

is χ-square distributed with two degrees of freedom. This implies that

$$\mathrm{std}\left(\tilde{Y}_j\right) = \mathrm{E}\left[\tilde{Y}_j\right] \ , \tag{S29}$$

i.e. , the standard deviation of the noise floor equals the expectation value of the noise floor. Using Parseval's theorem and again omitting a static offset, the standard deviation of the noise floor can also be related to the noise in the time trace,

$$\mathrm{std}\left(\tilde{Y}_j\right) = \mathrm{E}\left[\tilde{Y}_j\right] = \sum_{k=0}^{N-1} \mathrm{var}(\tilde{y}_k) \approx \sum_{k=0}^{N-1} \mathrm{var}(y_k) = N\sigma_y^2 \ . \tag{S30}$$

To obtain the SNR, we divide the expected signal $|\mathrm{E}\left[\hat{y}_j\right]|^2$ by the noise standard deviation $N\sigma_y^2$,

$$\mathrm{SNR} = \frac{|\mathrm{E}\left[\hat{y}_j\right]|^2}{N\sigma_y^2} = \frac{\mathrm{E}\left[Y_j\right] - N\sigma_y^2}{N\sigma_y^2} = \frac{\mathrm{E}\left[Y_j\right]}{N\sigma_y^2} - 1 \approx \frac{\mathrm{E}\left[Y_j\right]}{N\sigma_y^2} = \frac{\mathrm{E}\left[Y_j\right]}{\sigma_Y} \ , \tag{S31}$$

where the approximation is for large SNR, which was the case in our measurements. This corresponds to Eq. (4) in the main manuscript.

In a next step, we explicitly calculate the SNR that applies to our detection scheme. The expected a.c. signal contribution is given by

$$\begin{aligned}
|\mathrm{E}\left[\hat{y}_j\right]|^2 &= \left|\mathrm{E}\left[\sum_{k=0}^{N-1} y_k e^{-2\pi i k j}\right]\right|^2 && \text{(S32)}\\
&= \left|\sum_{k=0}^{N-1} \mathrm{E}\left[y_k\right] e^{-2\pi i k j}\right|^2 && \text{(S33)}\\
&= \left|\sum_{k=0}^{N-1} C\epsilon\, p(t_k) e^{-2\pi i k j}\right|^2 && \text{(S34)}\\
&= \left|\sum_{k=0}^{N-1} C\epsilon\, \frac{1}{2}\phi_k e^{-2\pi i k j}\right|^2 && \text{(S35)}\\
&= \frac{1}{4}\left(C\epsilon\right)^2 \left|\hat{\phi}_j\right|^2 , && \text{(S36)}
\end{aligned}$$

where we have omitted static offsets in Eq. (S34) and Eq. (S35) that only contribute to the $j = 0$ component. Here, $\hat{\phi}_j$ are Fourier components of the phases ϕ_k acquired by the quantum lock-in instances. We find that the signal power is proportional to the square of the readout gain C and the square of the optical contrast ϵ.

The noise variance σ_y^2 is calculated from Eq. (3) in the main manuscript, which includes two random processes, a Bernoulli process associated with the quantum state projection and a Poisson process associated with the photon shot noise. Both processes contribute to the noise variance. To compute the contribution by the Bernoulli process, we assume that the state probability $p(t_k)$ is oscillating closely around the $p = 0.5$ bias point. Then, the variance in p is $\frac{1}{4}$ and the corresponding variance in y_k is $\frac{1}{4}(C\epsilon)^2$. The contribution by the Poisson process has a variance that is equal to the mean of y_k, which is $\frac{1}{2}C(1-\epsilon/2)$. The total noise variance σ_y^2 is then

$$\sigma_y^2 = \frac{1}{4}C^2\epsilon^2 + C\left(1 - \frac{\epsilon}{2}\right) . \tag{S37}$$

This yields the explicit expression for the SNR,

$$\mathrm{SNR} = \frac{\frac{1}{4}(C\epsilon)^2|\hat{\phi}|^2}{N\left[\frac{1}{4}(C\epsilon)^2 + C(1-\frac{\epsilon}{2})\right]} = \frac{\frac{1}{4}(C\epsilon)^2\, N}{\frac{1}{4}(C\epsilon)^2 + C(1-\frac{\epsilon}{2})}|\hat{\phi}_j/N|^2 . \tag{S38}$$

This SNR applies to a general Fourier component of the spectrum Y_j. If the spectrum has very narrow peaks, such that the entire signal power is concentrated in a single Fourier component Y_j, we have

$$|\hat{\phi}_j/N|^2 = \frac{1}{4}\phi_{\mathrm{max}}^2 . \tag{S39}$$

This situation corresponds to the case where the intrinsic linewidth γ_{int} of the signal is smaller than the frequency resolution δf, which is the typical situation for our experiments. In this situation, the SNR is

$$\mathrm{SNR} = \frac{\frac{1}{16}(C\epsilon)^2\, N\phi_{\mathrm{max}}^2}{\frac{1}{4}(C\epsilon)^2 + C(1-\frac{\epsilon}{2})} . \tag{S40}$$

This is Eq. (6) of the main manuscript. If the signal has only one frequency component and the lock-in is tuned to that frequency, $\phi_{\mathrm{max}} = 2t_{\mathrm{a}}\Omega/\pi$ (see Eq. (S9)).

Eq. (S40) represents the SNR for an ideal read-out process. In our experiments, the read out was compromised by the limited robustness of the nuclear ^{15}N quantum memory. With each quantum non-demolition (QND) measurement of the memory qubit, there is a finite chance of depolarizing the qubit and losing the stored information. Although this effect is rather weak in our case, with a spin flip probability per QND measurement of $\Gamma \lesssim 0.1\%$, it needs to be considered for large QND repetitions n.

Because the depolarization probability is small, we can restrict ourselves to the following two cases: Either there are zero nuclear spin flips during readout, or there is a non-zero number of spin flips. In the first case, the original state is detected during the entire readout and we gain the correct information about the transition probability $p(t_k)$. By contrast, in the second case, the information is lost along the readout process. The probability distribution of photon counts y_k is given by

$$f\left(y_k | p\left(t_k\right)\right) = e^{-\Gamma n}\, f\left(y_k |\, p\left(t_k\right) \wedge \text{no flip}\,\right) + (1 - e^{-\Gamma n})\tilde{f}\left(y_k |\text{ flip }\right) . \tag{S41}$$

where n is the number of QND repetitions. We note that the probability distribution function $\tilde{f}\left(y_k |\text{ flip }\right)$ in the case of a non-zero number of spin flips is independent of the transition probability $p(t_k)$. Similar to

Eq. (S36), we can compute the expected power in the spectrum as

$$|\mathrm{E}\left[\hat{y}_j\right]|^2 = \frac{1}{4}(C\epsilon)^2\, e^{-2\Gamma n} \left|\hat{\phi}_j\right|^2 , \tag{S42}$$

This yields a modified SNR given by

$$\mathrm{SNR} = \frac{\frac{1}{16}(C\epsilon)^2\; N e^{-2\Gamma n}\phi^2_{\mathrm{max}}}{\frac{1}{4}(C\epsilon)^2 + C(1-\frac{\epsilon}{2})}\ . \tag{S43}$$

We have used this equation to fit the data in Fig. 4 of the main text and to extract values for the readout gain C, the optical contrast ϵ and the spin flip rate Γ.

Supplementary Text 4: Details of the compressive sampling protocol

Due to the nature of the lock-in measurement and the long sampling period t_s, we acquire sample records $\{y_k\}$ at rates $f_\mathrm{s} = 1/t_\mathrm{s}$ that are far below the Nyquist rate for the a.c. signals. This means that our continuous sampling strategy enables an arbitrarily fine frequency resolution only in a narrow bandwidth, and does not reproduce the absolute signal frequency. To reconcile the absolute signal frequency, we record the same a.c. signal several times with slightly different sampling rates f_s. In our detection scheme, we can adjust f_s by adding a small extra delay to the delay time t_d. We then reconstruct the wideband spectrum based on a compressive sampling (CS) technique *(17)*.

CS refers to the idea that certain types of signals, more exactly signals which are sparse in some basis, can be reconstructed out of a small number of partial measurements. Specifically, suppose that we have a discrete number of samples M of a signal $x(t)$ with $0 < t < T$. Then $x(t)$ can be represented by a set of basis functions $\varphi_k(t)$, for example the Fourier basis $\varphi_k(t) = e^{i2\pi f_k t}$, as

$$x(t) = \sum_{k=0}^{M-1} X_k \varphi_k(t) \ . \tag{S44}$$

If only a few coefficients X_k are significantly non-zero, then the signal $x(t)$ is considered *sparse* and its reconstruction from a set of measurements acquired at sub-Nyquist rates becomes an optimization problem *(17, 36)*.

Let us assume that the signal is represented by the vector $\vec{x} = \{x_0, \ldots, x_m, \ldots, x_M\}$ and that the samples of $\vec{x}$ are acquired at or above a relevant Nyquist rate. Then the discrete wideband spectrum $\vec{X} = \{X_0, \ldots, X_k, \ldots, X_M\}$ of $\vec{x}$ is given by the set of coefficients X_k,

$$X_k = \sum_{m=0}^{M-1} x_m \exp\left(-i2\pi k \frac{m}{M}\right) \ , \tag{S45}$$

The process of measuring an undersampled spectrum $\vec{Y_i}$ of $\vec{X}$ can be viewed as the action of a sampling matrix Φ_i on the target spectrum $\vec{X}$. If each partial measurement $\vec{Y_i}$ consists of N_i samples, then each Φ_i has dimensions $N_i \times M$. It has been shown that $\vec{X}$ can be recovered by using $p \approx s\mathcal{O}(\log(M))$ partial measurements where $s \ll M$ indicates the sparsity of $\vec{X}$, *i.e.* the number of significantly non-zero coefficients of $\vec{X}$ *(37)*. The problem can be written as

$$\vec{\boldsymbol{Y}} = \begin{pmatrix} \vec{Y_1} \\ \vdots \\ \vec{Y_p} \end{pmatrix} = \begin{pmatrix} \Phi_1 \\ \vdots \\ \Phi_p \end{pmatrix} \vec{X} = \boldsymbol{\Phi}\vec{X}, \tag{S46}$$

where $\vec{\boldsymbol{Y}}$ is a vector that contains the p undersampled spectra $\vec{Y_i}$ and $\boldsymbol{\Phi}$ a vector that contains the p sampling matrices Φ_i of dimensions $N_i \times M$ each. Thus, reconstruction of $\vec{X}$ out of the set of $\vec{Y_i}$ requires appropriate construction of the sampling matrices Φ_i and dedicated algorithms. The problem has motivated research in the context of wideband spectrum sensing *(38)*, where the idea is to achieve awareness of spectral opportunities, *i.e.* , to detect and fill licensed but unused portions of the electromagnetic spectrum at minimal computational cost. For this purpose, approaches like l_1 minimization or greedy pursuit algorithms have been studied *(23, 39)*.

In our experiment, we implemented a compressive sensing scheme where the $\vec{Y}_i$ represent undersampled spectra acquired at slightly different sampling rates $f_{\mathrm{s}}^{(i)}$. We varied the sampling rates by adding small extra delays to the delay time t_{d}. We then constructed a sampling matrix Φ_i for each spectrum $\vec{Y}_i$ following Refs. *(23, 39)* and solved the linear system (Eq. S46) by a non-negative linear least-squares solver (`lsqnonneg`) in Matlab.

To successfully reconstruct $\vec{X}$, suitable sampling matrices Φ_i need to be chosen. The reason is that we want to avoid that two matrices Φ_i and Φ_j map the same components of $\vec{X}$ into different undersampled spectra $\vec{Y}_i$ and $\vec{Y}_j$. To avoid such a situation, the matrices should be chosen as orthogonal or maximally incoherent as possible. The coherence μ of the sampling matrices is obtained via the inner product of their columns

$$\mu = \max_{i \neq j \in [1,M]} |\langle \phi_i, \phi_j \rangle| \tag{S47}$$

where ϕ_i denotes a l_2-normalized column of the matrix $\boldsymbol{\Phi}$. μ is a measure of the orthogonality of the sampling matrices, and under appropriate construction equals $1/p$ *(23)*. In such case, the spectrum $\vec{X}$ can be exactly reconstructed if $p > 2s - 1$ *(17)*.

We minimized the coherence of our sampling matrices by choosing random delay times t_{d}, which in turn determine $f_{\mathrm{s}}^{(i)}$ and therefore $N_i = T f_{\mathrm{s}}^{(i)}$. Furthermore, since the effective total measurement durations $T_i \approx T$ were not identical (due to rounding requirements of the pulse generator), the frequency resolution for a measured $\vec{Y}_i$ and the sought after spectrum $\vec{X}$ are not exactly the same. We therefore interpolated the elements of the sampling matrices Φ_i, which would ideally be $\in \{0, 1\}$, to fractional values $\in [0...1]$, as

$$\begin{aligned}
\Phi_i\left[n', m'\right] &= \frac{N_i}{M} \sum_{l=-\infty}^{\infty} w_{nm} \left(\delta\left(m - \left\lfloor (n + lN_i) \frac{T}{T_i} \right\rfloor \right) + \delta\left(m - \left\lceil (n + lN_i) \frac{T}{T_i} \right\rceil \right) \right) \\
n' &= n + \left\lfloor \frac{N_i}{2} \right\rfloor + 1 \\
m' &= m + \left\lfloor \frac{M}{2} \right\rfloor + 1 \\
w_{nm} &= \left| 1 - \left(m - (n + lN_i) \frac{T}{T_i} \right) \right|
\end{aligned}$$

where $\lfloor a \rfloor$ is the floor function and $\lceil a \rceil$ is the ceil function. $\delta(a)$ denotes the Kronecker delta function and $|a|$ the absolute value. To minimize computational costs, we only reconstructed the portions of the spectrum falling within the CPMG filter windows, *i.e.* , we constructed sparse matrices Φ_i with zeros everywhere outside the spectral portions of interest.

Supplementary Figure 1

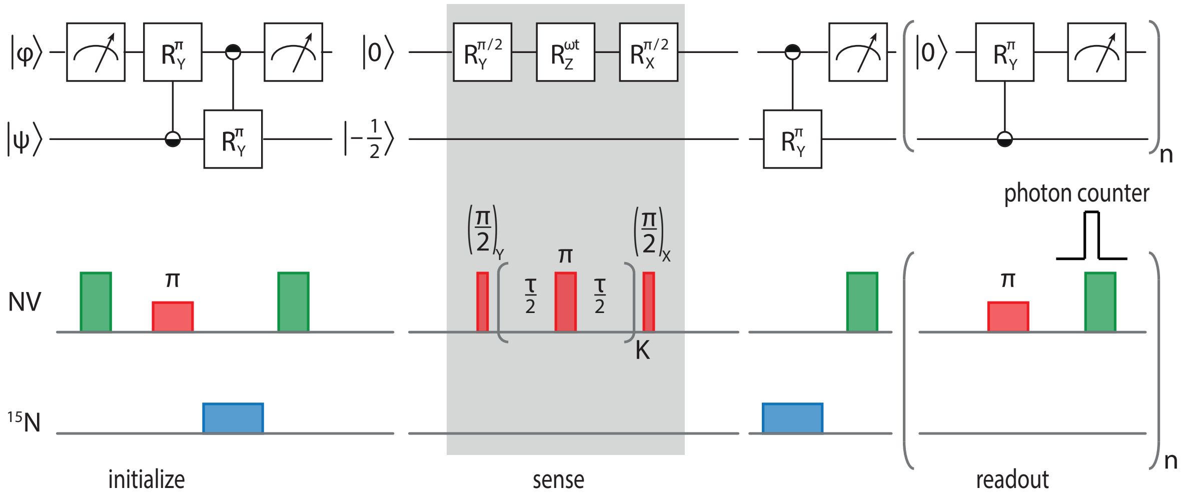

FIG. S1: Qubit gate diagram of one sensing instance. Two qubits were used, including a probe qubit (implemented by the electronic spin of the NV center) and a memory qubit (implemented by the ^{15}N nuclear spin of the NV center). The top channel represents the electronic and the bottom channel the nuclear qubit. The nuclear spin was initialized by a laser pulse (green) plus two c-NOT gates. Thereafter, the electronic qubit was initialized by another laser pulse. The c-NOT gates were implemented by selective microwave (red) and radio-frequency (blue) inversion pulses on the electronic and nuclear hyperfine transitions, respectively. A CPMG sequence adjusted to the frequency of interest was then executed on the electronic qubit. The resulting state was stored in the nuclear qubit via another c-NOT gate and subsequently read out in a repetitive quantum-nondemolition measurement *(21)*. The readout sequence consisted of the repetitive execution of an electronic c-NOT gate followed by a readout laser pulse of duration ≈800 ns. Full-height pulses symbolize non-selective pulses and half-height pulses symbolize selective pulses.

Supplementary Figure 2

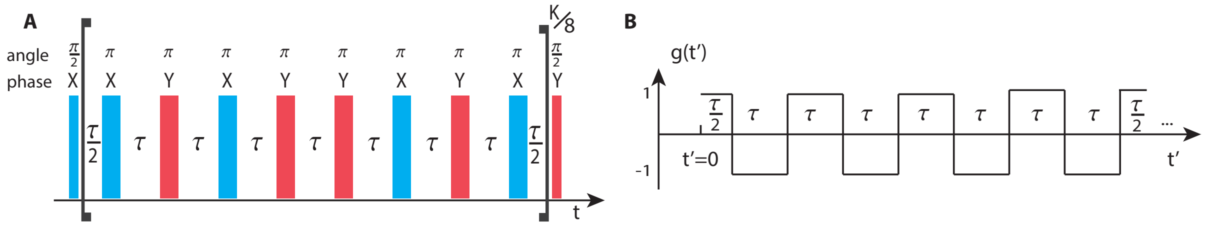

FIG. S2: (**A**) Pulse timing diagram of the CPMG sequence executed on the electronic qubit. Blue (red) microwave pulses stand for rotations around the X-axis (Y-axis). The eight π-pulses in the square bracket are repeated $\frac{K}{8}$ times. The alternation of the rotation axes is that of an XY8 sequence *(40)*. (**B**) Modulation function $g(t)$ of the CPMG sequence. Each π reverts the accumulated quantum phase of the qubit, represented by a change in sign of the modulation function.

Supplementary Figure 3

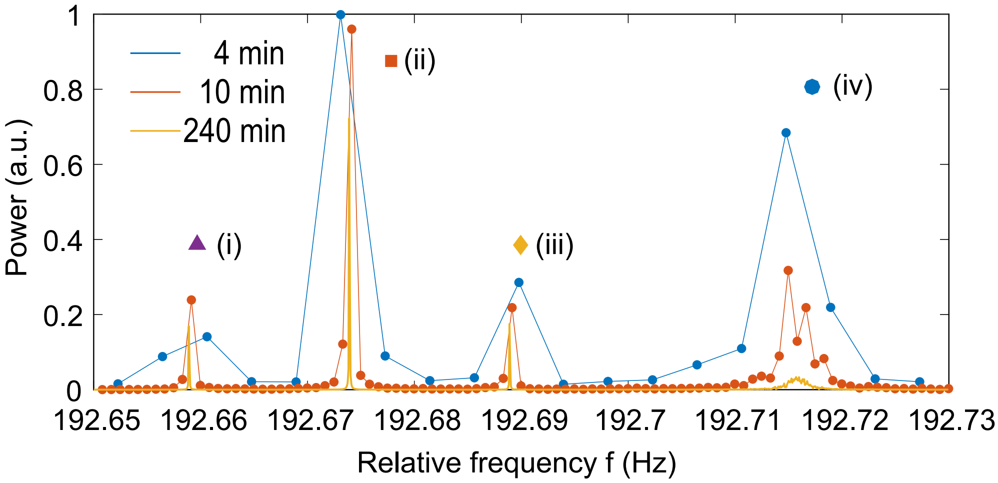

FIG. S3: Power spectrum of a.c. signals for $T = 4\,\mathrm{min}$, $10\,\mathrm{min}$ and $240\,\mathrm{min}$. Peaks (i-iii) originate from coherent signals at $f_\mathrm{c} = 1.2\,\mathrm{MHz}$ and $f_\mathrm{c} \pm 15\,\mathrm{mHz}$ produced by amplitude modulation. Signal (iv) with frequency $f_\mathrm{c} + 40\,\mathrm{mHz}$ originates from a frequency modulated (FM) signal with an artificial line broadening of $\gamma_\mathrm{int} = 0.76\,\mathrm{mHz}$.

Supplementary Figure 4

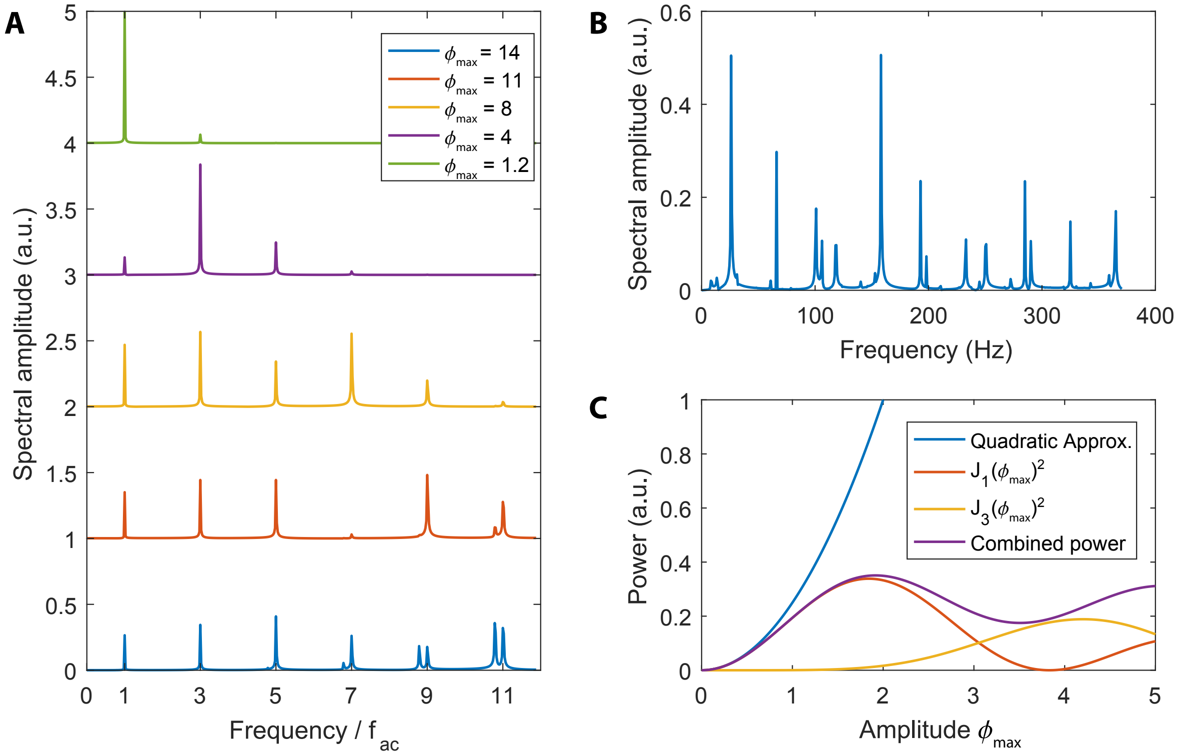

FIG. S4: (**A**) Simulated spectra based on formula given in Eq. (S11) for different signal amplitudes ϕ_{max}. Odd harmonics of the signal frequency f_{ac} are observed as ϕ_{max} exceeds the linear regime of the sensor ($\phi_{\mathrm{max}} \gtrsim 1$). The number of harmonics increases with the signal amplitude ϕ_{max}, eventually leading to spectral folding. (**B**) Simulated spectrum of a signal with two frequency components: $f_{\mathrm{ac}} = 400.75$ kHz and $f'_{\mathrm{ac}} = 401.75$ kHz sampled at a rate of $f_{\mathrm{s}} = 742.1$ Hz. The signal amplitudes are $\phi_{\mathrm{max},1} = 3$ and $\phi_{\mathrm{max},2} = 2$, respectively. The spectrum shows harmonics as well as frequency mixing of the two fundamental frequencies. Spectral folding further complicates the interpretation of the spectrum. (**C**) Peak height in the power spectrum as a function of ϕ_{max} for a signal with frequency f_{ac}. The blue curve is given by $\phi_{\mathrm{rms}}^2/4$ and represents the linear regime where $J_1(\phi_{\mathrm{max}}) \approx \phi_{\mathrm{max}}/2$. We have used this approximation in our experiments. The red and yellow curves show the first and third Bessel function corresponding to the amplitudes of the f_{ac} and $3f_{\mathrm{ac}}$ harmonics, respectively. The purple curve shows the total power of all harmonics, $\sum_{k=0}^{\infty} J_{2k+1}^2(\phi_{\mathrm{max}})$, which approaches 0.25 as $\phi_{\mathrm{max}} \to \infty$.

Supplementary Figure 5

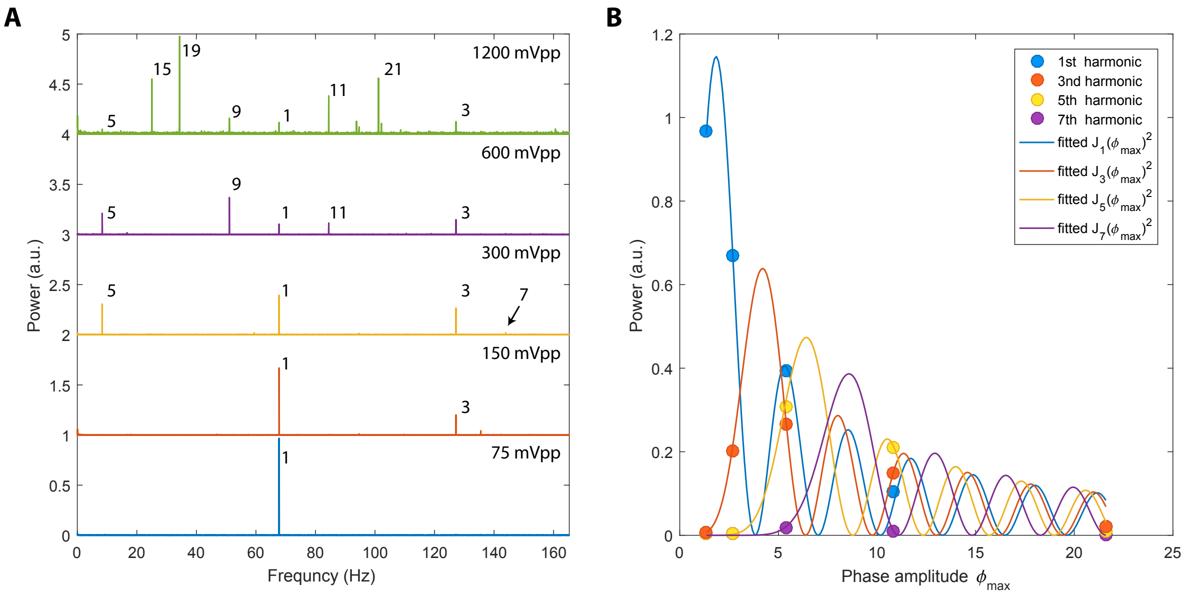

FIG. S5: (**A**) Experimental spectra of a single tone a.c. signal with $f_{\mathrm{ac}} = 1.202254655\,\mathrm{MHz}$ for five different amplitude settings on the external signal generator. The amplitude settings are stated with each plot. The spectra are vertically shifted by one unit for clarity. All spectra use the same vertical scale, except for the top spectrum which is magnified $6\times$. Labels identify the different signal harmonics as discussed with Eq. (S11). (**B**) Fitted peak heights for the first four harmonics at f_{ac}, $3f_{\mathrm{ac}}$, $5f_{\mathrm{ac}}$ and $7f_{\mathrm{ac}}$ as a function of the phase amplitude ϕ_{max}. The data are in excellent agreement with Eq. (S11).

References and Notes

1. V. Giovannetti, S. Lloyd, L. Maccone, Advances in quantum metrology. *Nat. Photonics* **5**, 222–229 (2011). doi:10.1038/nphoton.2011.35
2. C. L. Degen, F. Reinhard, P. Cappellaro, Quantum sensing. arXiv:1611.02427 [quant-ph] (8 November 2016).
3. M. W. Doherty, N. B. Manson, P. Delaney, F. Jelezko, J. Wrachtrup, L. C. L. Hollenberg, The nitrogen-vacancy colour centre in diamond. *Phys. Rep.* **528**, 1–45 (2013). doi:10.1016/j.physrep.2013.02.001
4. J. J. Pla, K. Y. Tan, J. P. Dehollain, W. H. Lim, J. J. L. Morton, D. N. Jamieson, A. S. Dzurak, A. Morello, A single-atom electron spin qubit in silicon. *Nature* **489**, 541–545 (2012). doi:10.1038/nature11449 Medline
5. M. Widmann, S.-Y. Lee, T. Rendler, N. T. Son, H. Fedder, S. Paik, L.-P. Yang, N. Zhao, S. Yang, I. Booker, A. Denisenko, M. Jamali, S. A. Momenzadeh, I. Gerhardt, T. Ohshima, A. Gali, E. Janzén, J. Wrachtrup, Coherent control of single spins in silicon carbide at room temperature. *Nat. Mater.* **14**, 164–168 (2015). doi:10.1038/nmat4145 Medline
6. R. Kolesov, K. Xia, R. Reuter, R. Stöhr, A. Zappe, J. Meijer, P. R. Hemmer, J. Wrachtrup, Optical detection of a single rare-earth ion in a crystal. *Nat. Commun.* **3**, 1029 (2012). doi:10.1038/ncomms2034 Medline
7. G. Balasubramanian, I. Y. Chan, R. Kolesov, M. Al-Hmoud, J. Tisler, C. Shin, C. Kim, A. Wojcik, P. R. Hemmer, A. Krueger, T. Hanke, A. Leitenstorfer, R. Bratschitsch, F. Jelezko, J. Wrachtrup, Nanoscale imaging magnetometry with diamond spins under ambient conditions. *Nature* **455**, 648–651 (2008). doi:10.1038/nature07278 Medline
8. P. Maletinsky, S. Hong, M. S. Grinolds, B. Hausmann, M. D. Lukin, R. L. Walsworth, M. Loncar, A. Yacoby, A robust scanning diamond sensor for nanoscale imaging with single nitrogen-vacancy centres. *Nat. Nanotechnol.* **7**, 320–324 (2012). doi:10.1038/nnano.2012.50 Medline
9. S. Kotler, N. Akerman, Y. Glickman, A. Keselman, R. Ozeri, Single-ion quantum lock-in amplifier. *Nature* **473**, 61–65 (2011). doi:10.1038/nature10010 Medline
10. G. de Lange, D. Ristè, V. V. Dobrovitski, R. Hanson, Single-spin magnetometry with multipulse sensing sequences. *Phys. Rev. Lett.* **106**, 080802 (2011). doi:10.1103/PhysRevLett.106.080802 Medline
11. G. A. Álvarez, D. Suter, Measuring the spectrum of colored noise by dynamical decoupling. *Phys. Rev. Lett.* **107**, 230501 (2011). doi:10.1103/PhysRevLett.107.230501 Medline
12. F. Yan, S. Gustavsson, J. Bylander, X. Jin, F. Yoshihara, D. G. Cory, Y. Nakamura, T. P. Orlando, W. D. Oliver, Rotating-frame relaxation as a noise spectrum analyser of a superconducting qubit undergoing driven evolution. *Nat. Commun.* **4**, 2337 (2013). doi:10.1038/ncomms3337 Medline
13. M. Loretz, T. Rosskopf, C. L. Degen, Radio-frequency magnetometry using a single electron spin. *Phys. Rev. Lett.* **110**, 017602 (2013). doi:10.1103/PhysRevLett.110.017602 Medline
14. J. E. Lang, R. B. Liu, T. S. Monteiro, Dynamical-decoupling-based quantum sensing: Floquet spectroscopy. *Phys. Rev. X* **5**, 041016 (2015). doi:10.1103/PhysRevX.5.041016

15. A. Laraoui, F. Dolde, C. Burk, F. Reinhard, J. Wrachtrup, C. A. Meriles, High-resolution correlation spectroscopy of ^{13}C spins near a nitrogen-vacancy centre in diamond. *Nat. Commun.* **4**, 1651 (2013). doi:10.1038/ncomms2685 Medline

16. S. Zaiser, T. Rendler, I. Jakobi, T. Wolf, S.-Y. Lee, S. Wagner, V. Bergholm, T. Schulte-Herbrüggen, P. Neumann, J. Wrachtrup, Enhancing quantum sensing sensitivity by a quantum memory. *Nat. Commun.* **7**, 12279 (2016). doi:10.1038/ncomms12279 Medline

17. D. L. Donoho, Compressed sensing. *IEEE Trans. Inf. Theory* **52**, 1289–1306 (2006). doi:10.1109/TIT.2006.871582

18. L. Rondin, J.-P. Tetienne, T. Hingant, J.-F. Roch, P. Maletinsky, V. Jacques, Magnetometry with nitrogen-vacancy defects in diamond. *Rep. Prog. Phys.* **77**, 056503 (2014). doi:10.1088/0034-4885/77/5/056503 Medline

19. R. Schirhagl, K. Chang, M. Loretz, C. L. Degen, Nitrogen-vacancy centers in diamond: Nanoscale sensors for physics and biology. *Annu. Rev. Phys. Chem.* **65**, 83–105 (2014). doi:10.1146/annurev-physchem-040513-103659 Medline

20. S. Kotler, N. Akerman, Y. Glickman, R. Ozeri, Nonlinear single-spin spectrum analyzer. *Phys. Rev. Lett.* **110**, 110503 (2013). doi:10.1103/PhysRevLett.110.110503 Medline

21. L. Jiang, J. S. Hodges, J. R. Maze, P. Maurer, J. M. Taylor, D. G. Cory, P. R. Hemmer, R. L. Walsworth, A. Yacoby, A. S. Zibrov, M. D. Lukin, Repetitive readout of a single electronic spin via quantum logic with nuclear spin ancillae. *Science* **326**, 267–272 (2009). doi:10.1126/science.1176496 Medline

22. P. Neumann, J. Beck, M. Steiner, F. Rempp, H. Fedder, P. R. Hemmer, J. Wrachtrup, F. Jelezko, Single-shot readout of a single nuclear spin. *Science* **329**, 542–544 (2010). doi:10.1126/science.1189075 Medline

23. H. Sun, W.-Y. Chiu, J. Jiang, A. Nallanathan, H. V. Poor, Wideband spectrum sensing with sub-Nyquist sampling in cognitive radios. *IEEE Trans. Signal Process.* **60**, 6068–6073 (2012). doi:10.1109/TSP.2012.2212892

24. H. J. Mamin, M. Kim, M. H. Sherwood, C. T. Rettner, K. Ohno, D. D. Awschalom, D. Rugar, Nanoscale nuclear magnetic resonance with a nitrogen-vacancy spin sensor. *Science* **339**, 557–560 (2013). doi:10.1126/science.1231540 Medline

25. T. Staudacher, F. Shi, S. Pezzagna, J. Meijer, J. Du, C. A. Meriles, F. Reinhard, J. Wrachtrup, Nuclear magnetic resonance spectroscopy on a (5-nanometer)^3 sample volume. *Science* **339**, 561–563 (2013). doi:10.1126/science.1231675 Medline

26. J. M. Cai, A. Retzker, F. Jelezko, M. B. Plenio, A large-scale quantum simulator on a diamond surface at room temperature. *Nat. Phys.* **9**, 168–173 (2013). doi:10.1038/nphys2519

27. M. Mehring, *Principles of High Resolution NMR in Solids* (Springer, 2012).

28. B. Reif, Ultra-high resolution in MAS solid-state NMR of perdeuterated proteins: Implications for structure and dynamics. *J. Magn. Reson.* **216**, 1–12 (2012). doi:10.1016/j.jmr.2011.12.017 Medline

29. S. Appelt, H. Kuhn, F. W. Hasing, B. Blumich, Chemical analysis by ultrahigh-resolution nuclear magnetic resonance in the Earth’s magnetic field. *Nat. Phys.* **2**, 105–109 (2006). doi:10.1038/nphys211

30. See supplementary materials.

31. T. M. Babinec, B. J. M. Hausmann, M. Khan, Y. Zhang, J. R. Maze, P. R. Hemmer, M. Lončar, A diamond nanowire single-photon source. *Nat. Nanotechnol.* **5**, 195–199 (2010). doi:10.1038/nnano.2010.6 Medline

32. S. A. Momenzadeh, R. J. Stöhr, F. F. de Oliveira, A. Brunner, A. Denisenko, S. Yang, F. Reinhard, J. Wrachtrup, Nanoengineered diamond waveguide as a robust bright platform for nanomagnetometry using shallow nitrogen vacancy centers. *Nano Lett.* **15**, 165–169 (2015). doi:10.1021/nl503326t Medline

33. N. Aslam, G. Waldherr, P. Neumann, F. Jelezko, J. Wrachtrup, Photo-induced ionization dynamics of the nitrogen vacancy defect in diamond investigated by single-shot charge state detection. *New J. Phys.* **15**, 013064 (2013). doi:10.1088/1367-2630/15/1/013064

34. F. Jelezko, J. Wrachtrup, Single defect centres in diamond: A review. *Phys. Status Solidi., A Appl. Mater. Sci.* **203**, 3207–3225 (2006). doi:10.1002/pssa.200671403

35. T. Rosskopf, J. Zopes, J. M. Boss, C. L. Degen, A quantum spectrum analyzer enhanced by a nuclear spin memory. arXiv:1610.03253 [quant-ph] (11 October 2016).

36. E. J. Candes, J. Romberg, T. Tao, Robust uncertainty principles: Exact signal reconstruction from highly incomplete frequency information. *IEEE Trans. Inf. Theory* **52**, 489–509 (2006). doi:10.1109/TIT.2005.862083

37. Y. L. Polo, W. Ying, A. Pandharipande, G. Leus, Compressive Wide-band Spectrum Sensing. 2337–2340 (2009).

38. C. Nader, N. Bjorsell, P. Handel, Unfolding the frequency spectrum for undersampled wideband data. *Signal Process.* **91**, 1347–1350 (2011). doi:10.1016/j.sigpro.2010.12.013

39. D. Needell, J. A. Tropp, CoSaMP: Iterative signal recovery from incomplete and inaccurate samples. *Commun. ACM* **53**, 93–100 (2010). doi:10.1145/1859204.1859229

40. T. Gullion, D. B. Baker, M. S. Conradi, New, compensated Carr-Purcell sequences. *J. Magn. Reson.* **89**, 479–484 (1990).